Spin dynamics of exchange-coupled nitrogen donors in heavily doped *n*-type 15*R* SiC monocrystals: Multifrequency EPR and EDMR study

A. Solodovnyk,[1] O. Laguta,[1] A. Prokhorov,[2] M. Segantini,[3] B. Naydenov,[3] P. Neugebauer,[1] S. Greulich-Weber,[4] E. Kalabukhova,[5] and D. Savchenko[2,6,*]

[1]*Central European Institute of Technology, Brno University of Technology, Purkynova 656/123 Brno, 61200, Czech Republic*
[2]*Department of Analysis of Functional Materials, Institute of Physics of the CAS, Na Slovance 2, 18200, Prague 8, Czech Republic*
[3]*Berlin Joint EPR Laboratory, Department Spins in Energy Conversion and Quantum Information Science (ASPIN), Helmholtz-Zentrum Berlin für Materialien und Energie GmbH, Hahn-Meitner-Platz 1, Berlin, 14109, Germany*
[4]*The Yellow SiC Development GmbH, Schwarzschildstraße 1, D-12489 Berlin, Germany*
[5]*Department of optics and spectroscopy, V.E. Lashkaryov Institute of Semiconductor Physics NAS of Ukraine, pr. Nauky 41, Kyiv, 03028, Ukraine*
[6]*Department of General Physics and Modelling of Physical Processes, National Technical University of Ukraine "Igor Sikorsky Kyiv Polytechnic Institute", pr. Peremohy 37, Kyiv, 03056, Ukraine*

(Received 7 February 2023; accepted 29 March 2023; published 13 April 2023)

Semiconductor devices based on 15*R* silicon carbide (SiC) show improved properties compared to other polytypes. Here, we report the investigation of nitrogen-doped 15*R* SiC monocrystals with $(N_D–N_A) \sim 5\times10^{18}$ cm^{-3} using multifrequency electron paramagnetic resonance (EPR) and electrically detected magnetic resonance (EDMR) spectroscopic methods in the microwave (MW) frequency range from 9.4 to 328.84 GHz and in the temperature range from 4.2 to 300 K. A single intensive *S* line with $S = 1/2$, at $g_\perp = 2.0026(2)$, and $g_\parallel = 2.0043(2)$ dominates the EPR spectrum in 15*R* SiC at $T < 160$ K and was attributed to the exchange-coupled nitrogen (N) donors substituting quasicubic "*k*1" site having the deeper energy level in 15*R* SiC lattice. From the analysis of the temperature behavior of the integral intensity, magnetic field position, intensity, shape, and width of the *S* line, it was concluded that at $T < 90$ K, the exchange coupling occurs between localized donor electrons, while at $T = 90-150$ K the interaction between exchange-coupled N donors and conduction electrons takes place. In the temperature interval from 20 to 160 K, the *S*-line EPR width was characterized by a two-phonon Orbach relaxation process with the activation energy of ∼6.5 meV corresponding to the valley-orbit splitting values for N donors in 15*R* SiC. The variable-range hopping regime obeying the $T^{1/4}$ law was found to take place at $T < 20$ K leading to the appearance of the *S* line in the EDMR spectrum at low temperatures. The appearance of the EDMR signal from exchange-coupled N donors is caused by the EPR-induced temperature-increase mechanism and the spin-flip hops process. The results obtained from MW conductivity measurements agree with EPR and EDMR data. The temperature variation of MW conductivity was described by several processes, including the electron-hopping process between N donor impurity atoms at $T < 50$ K with activation energy $\varepsilon_3 = 1.5$ meV, electron transitions between Hubbard bands at $T = 50$–100 K; the transition of the electrons from the donor energy levels to conduction band with ionization energy $\varepsilon_1 = 32$ meV at $T = 100$–200 K and scattering of the conduction electrons by ionized donors occurred at the temperature higher than 200 K.

DOI: 10.1103/PhysRevB.107.155202

I. INTRODUCTION

The silicon carbide (SiC) crystals have numerous modifications due to various types of crystalline lattices that determine semiconductor material properties and atom properties. Various crystalline structures (polytypes) occurred due to different ways of layer ordering. SiC possesses over 250 polytypes, each providing exclusive electrical and optical properties caused by a different arrangement of the silicon (Si) and carbon (C) atoms within the crystalline lattice. The cubic (3C), hexagonal (4H, 6H), and rhombohedral (15*R*) polytypes of SiC are most commonly developed for applications in power electronic devices. Among them, the 15*R* polytype of SiC can enhance high-voltage SiC metal-oxide-semiconductor field-effect transistor (MOSFET) properties owing to its higher bulk mobility, low anisotropy, and higher inversion layer mobility of charge carriers as compared to 4H and 6H polytypes [1]. Recently it was reported that 15*R*-SiC-based Schottky barrier diodes might be a potential candidate for extreme environment fast-switching devices and UV photodetectors [2]. Moreover, the 3C SiC layers deposited on the 15*R* SiC substrates have lower twin densities than those deposited under identical technological conditions on the 6H SiC substrates [3] and possess high structural quality [4].

At the same time, compared to 3C, 4H, and 6H polytypes, the electronic structure of acceptors and donors in 15*R* SiC and their magnetic properties were less studied. Nitrogen (N)

*dariyasavchenko@gmail.com

donors in SiC are responsible for *n*-type conductivity; therefore, understanding their properties is crucial for applying SiC in high-power electronics.

Electron paramagnetic resonance (EPR) and electrically detected magnetic resonance (EDMR) spectroscopic techniques are widely used to investigate the electronic and magnetic properties of dopants in semiconductors, in particular in carbide materials [5,6]. The main difference between these methods is that the EPR method is based on absorption/dispersion of microwave (MW) and radio-frequency intensities, while in EDMR, the change in the sample's conductivity induced by magnetic resonance is detected.

Previous EPR and electron-nuclear double-resonance investigations of N-doped 15*R* SiC were performed in the monocrystals with $(N_D–N_A) \approx 10^{16}\,cm^{-3}$ of different stoichiometry [7,8], while no detailed EPR study of 15*R* SiC monocrystals with higher N donor concentration was reported.

At the same time, the previous EDMR study of SiC is mainly devoted to the interface and radiation-induced defects, Si vacancies, and C dangling bonds in 4H SiC/SiO_2 4H SiC MOSFETs, MOS, and transistors [9–20] and 6H SiC nanostructures [21]. Bulk SiC crystals were studied much less by the EDMR technique. For instance, in Ref. [22], the light-induced EDMR spectra of 4H SiC wafers were studied, and the observed signal at $g = 2.000(3)$ indicated that the vacancy acts as the major recombination center. Authors in Ref. [23] have established that $N_C V_{Si}^0$ is the dominant defect measured by spin-dependent recombination in N-implanted 4H SiC with $(N_D–N_A) \sim 5\times10^{17}\,cm^{-3}$. The results of the EDMR study of 6H SiC crystalline samples with $(N_D–N_A) \sim 10^{18}\,cm^{-3}$ presented in Ref. [24] allowed concluding that the EPR-induced temperature-increase mechanism causes the EDMR signal detected at low temperatures.

Recently in Ref. [25], some of us reported a single *S* line with $g_\perp = 2.0026(2)$ and $g_\parallel = 2.0043(2)$ in low-temperature EPR and EDMR spectra of 15*R* SiC with $(N_D–N_A) \sim 5\times10^{18}\,cm^{-3}$ that was assigned to the exchange interaction of N donors in 15*R* SiC via spin-dependent hopping process.

In this work, we report a detailed study of spin dynamics of the *S* line due to exchange-coupled N donors in 15*R* SiC with $(N_D–N_A) \sim 5\times10^{18}\,cm^{-3}$ in a wide temperature interval using contactless MW conductivity measurements, multifrequency continuous-wave EPR and EDMR methods. The mechanisms explaining the appearance of the EDMR signal from exchange-coupled N donors are discussed.

II. MATERIALS AND METHODS

The 15*R* SiC monocrystals with a nitrogen donor concentration of $(N_D–N_A) \sim 5\times10^{18}\,cm^{-3}$ were grown by the modified Lely method [26]. The sample size was about 3.4×0.8×0.4 mm. The typical crystal structure of the 15*R* polytype of SiC shown in Fig. 1 is characterized by stacking sequence ABCACBCABACABCB … and a hexagonality rate of 40%. There are five nonequivalent positions: three quasicubic *k*1, *k*2, and *k*3 and two hexagonal *h*1 and *h*2 in 15*R* SiC. As a result, the N donors in 15*R* SiC substitute these nonequivalent positions with donor energy levels in the band gap at ∼99 meV for $N_{k1,k2,k3}$ and ∼52 meV for $N_{h1,h2}$.

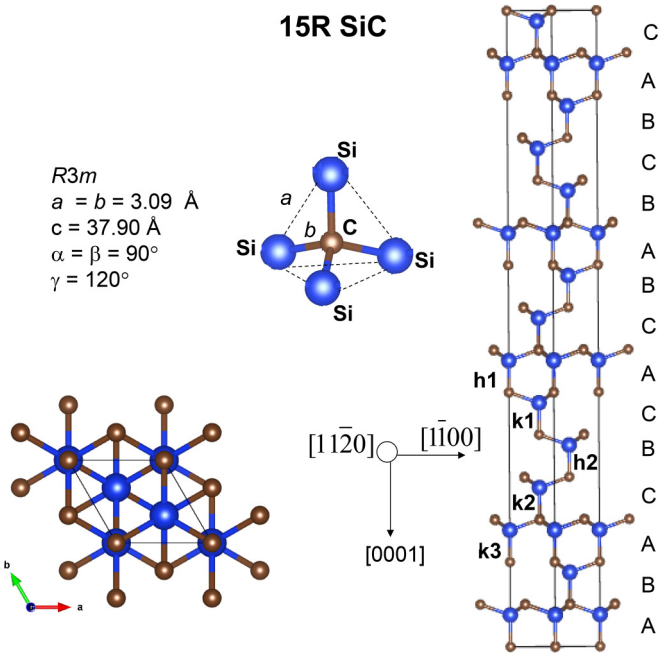

FIG. 1. Crystal structure of 15*R* SiC drawn in VESTA 3.5.2 program [27] using the data from Ref. [28] The **c** axis is along the [0001] direction.

X-band continuous-wave EPR, EDMR spectra, and MW conductivity were measured on the Bruker ELEXSYS E580 spectrometer in the temperature range 4.2–300 K. *X*-band ($\nu_0 \sim 9.4$ GHz) EPR spectra were recorded using Bruker ER 4122 SHQE superhigh-*Q* cylindrical TE_{011} cavity with ER 4112HV variable-temperature helium-flow cryostat. The following experimental conditions were used: microwave power level = 0.4743 mW, modulation frequency = 100 kHz, modulation amplitude = 0.5−1.0 mT (depending on the EPR linewidth), conversion time = 60 ms, and spectral resolution of 2048 points. The investigated crystals were placed on a 4-mm-diameter fused quartz rod. As a reference sample, we have used the 1,1-diphenyl-2-picrylhydrazyl free radical with $g = 2.0036$. The EPR spectra were simulated using the "pepper" function in the EASYSPIN 5.2.28 toolbox [29].

The temperature dependence of MW conductivity was measured using the so-called cavity perturbation method [30–33]: the parameters of the MW cavity are detected when the cavity is loaded with a sample with a smaller volume than the cavity volume. The *Q* factor of the unloaded and loaded cavity was obtained at a MW power level of 0.075 18 mW (33 dB).

X-band EDMR spectra were measured using Bruker Dielectric Ring Resonator ER 4118X-MD5W1 cavity with Oxford CF9350 variable-temperature helium-flow cryostat. The following experimental conditions were used: microwave power level = 15 mW, modulation frequency = 1350 Hz, modulation amplitude = 0.25 mT, sweep time = 40.959 76 s, lock-in conversion time = 40 ms, and spectral resolution of 1024 points. High-frequency EPR and EDMR spectra were measured on THz FraScan spectrometer (located in CEITEC BUT, Brno, Czech Republic). High-frequency EPR and EDMR spectra at 100 and 328.84 GHz were measured using one THz EDMR sample holder and two different microwave

sources. Magnetic field domain EPR spectra were measured using the following parameters: magnetic field (provided by superconductive cryogen-free magnet, Cryogenic Ltd, UK) sweep rate: 0.18 mT/s; lock-in (Zurich Instruments MFLI-500, Zurich, Switzerland), time constant: 30 ms; magnetic field modulation amplitude: 0.25 mT; magnetic field modulation frequency: 2.9 kHz; microwave power ∼1 mW. High-frequency magnetic field domain EDMR spectra were obtained using following parameters: magnetic field sweep rate: 0.18 mT/s; time constant: 30 ms; magnetic field modulation amplitude: 0.25 mT; magnetic field modulation frequency: 771 Hz; bias voltage: +4.8 V; microwave power: ∼125 mW (100 GHz), and ∼70 mW (328.84 GHz). For EDMR measurements the sample was contacted with Ag-based paint (Plano GmbH, Germany) onto glass substrate with Au contact pads.

III. RESULTS AND DISCUSSION

A. Contactless MW conductivity measurements

It is well known that by measuring the temperature dependence of resonance frequency shift δ and MW loss (Δ), one can estimate the temperature variation of MW conductivity (σ_{MW}) of the sample loaded in TE_{011} mode cavity as [34–36]

$$\sigma_{\mathrm{MW}} = 2\pi\nu_L\varepsilon_0 \frac{\frac{A}{N^2}\frac{\Delta}{2}}{\left(\frac{A}{N}-\delta\right)^2+\left(\frac{\Delta}{2}\right)^2}, \tag{1}$$

where $\delta = (\nu_0 - \nu_{\mathrm{L}})/\nu_0$, ν_0 and ν_L are the resonance frequency values of the unloaded and sample-loaded cavity, respectively, $\Delta = Q_L^{-1} + Q_0^{-1}$, Q_0 and Q_L are the quality-factor values of the unloaded and sample-loaded cavity, respectively, $\varepsilon_0 = 8.854\times10^{-12}$ F/m is the vacuum dielectric permittivity, $A =$ filling factor (for TE_{011} mode cavity $A = 2V_{\mathrm{S}}/V_{\mathrm{C}}$, where V_{S}– is the volume of the sample, V_{C} is the volume of the cavity), $N = -A\nu_L/\delta$ is the depolarization factor.

The temperature variation of microwave loss (Δ) and frequency shift (δ) in the investigated 15*R* SiC monocrystals is shown in Fig. 2(a). The corresponding dependence of the natural logarithm of MW conductivity calculated from Eq. (1) versus 1000/*T* is represented in Fig. 2(b).

It is well known that the temperature variation of the conductivity in highly-doped *n*-type semiconductors in the general case is described by the sum of four contributions [37–39]:

$$\sigma(T) = \sigma_1 \exp\left(\frac{-\varepsilon_1}{k_B T}\right) + \sigma_2 \exp\left(\frac{-\varepsilon_2}{k_B T}\right) + \sigma_3 \exp\left(\frac{-\varepsilon_3}{k_B T}\right) + \sigma_{\mathrm{VRH}}, \tag{2}$$

where the first term is related to conduction-band conductivity with the ionization energy of donors ε_1, ε_2 is the activation energy needed to take an electron from the lower Hubbard band to the mobility edge of the upper one, ε_3 is the activation energy for electron hopping from an occupied donor to an unoccupied one; the last term describes the variable-range hopping (VRH) conductivity.

From Fig. 2, it follows that in the temperature interval from 295 to 200 K, the conductivity grows slightly owing

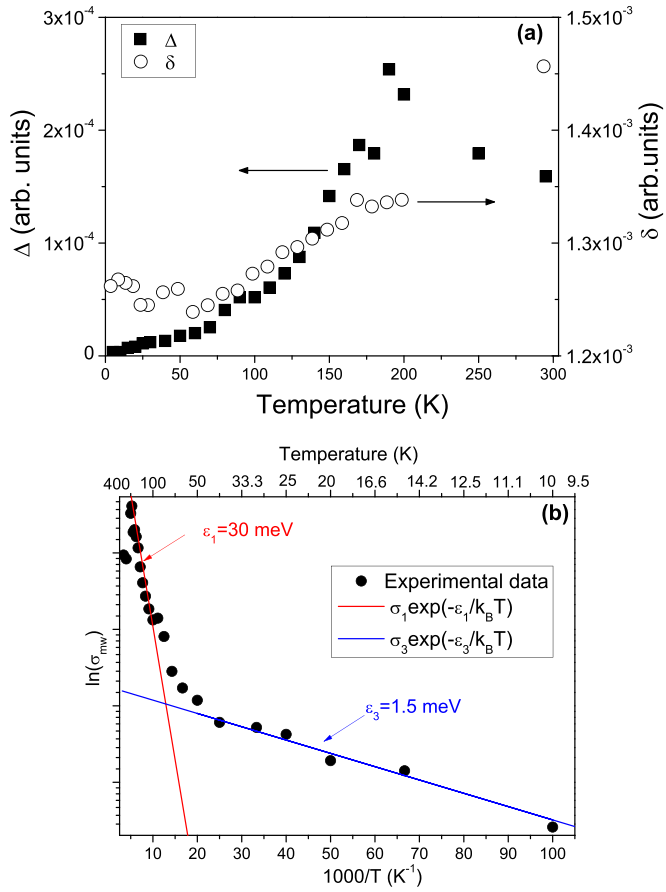

FIG. 2. (a) Temperature dependence of MW loss (Δ) and frequency shift (δ) measured in 15*R* SiC monocrystals with $(N_{\mathrm{D}}–N_{\mathrm{A}}) \sim 5\times10^{18}\ \mathrm{cm}^{-3}$. (b) Temperature dependence of the natural logarithm of MW conductivity estimated from Eq. (1). Dots are experimental data; solid red and blue lines represent the result of fitting with Eq. (2).

to the scattering of conduction electrons by ionized donor impurities [40].

In the temperature range from 200 to 100 K, the transitions of electrons from donor energy levels to the conduction band occur. This process is described by the first term of Eq. (2) related to conduction-band conductivity with ε_1.

Afterward, at $T = 100$–50 K, the transition process of electrons between Hubbard bands can occur in lightly compensated materials close to the Mott transition [second term in Eq. (2)] [40].

Finally, at $T < 50$ K, the electron-hopping process between donor impurity atoms appears, and the hopping conduction takes place with the activation energy ε_3. This process should be related to "nearest-neighbor hopping" or "thermally activated hopping," and the ε_3 value depends on the degree of compensation ($N_{\mathrm{A}}/N_{\mathrm{D}}$) and major impurity concentration [41–43].

From the fitting of experimental data with Eq. (2), we have found the following activation energy values for the main processes responsible for the temperature dependence of the MW conductivity: $\varepsilon_1 = 30$ meV and $\varepsilon_3 = 1.5$ meV. The obtained values agree well with those reported in Ref. [44] deduced

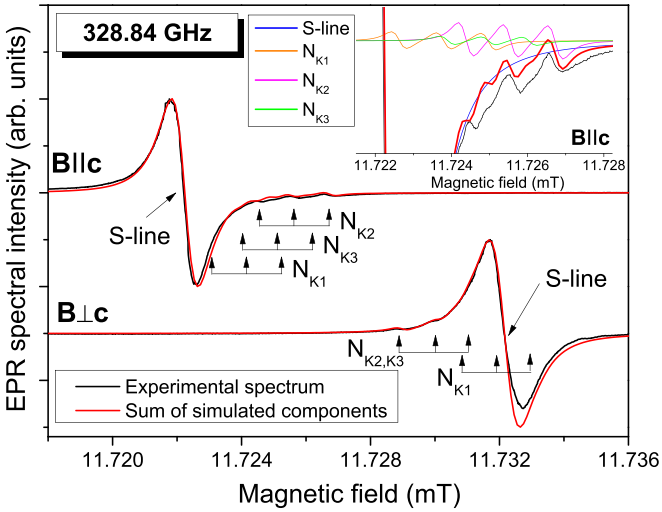

FIG. 3. High-frequency EPR spectra ($\nu_0 = 328.84$ GHz) measured in 15*R* SiC monocrystals having $(N_D–N_A) \sim 5\times10^{18}$ cm^{-3} at **B**‖**c** and **B**⊥**c** ($T = 8$ K). Solid black lines are experimental spectra; solid red lines are the sum of simulated components. Inset shows the detailed view of simulated components at **B**‖**c**.

from the temperature-dependent Hall measurements in 15*R* SiC crystals with $(N_D–N_A) > 10^{17}$ cm^{-3}: $\varepsilon_1 = 32$ meV and $\varepsilon_3 = 3$–4 meV. The obtained lower ε_1 value than that reported for N donor energy levels in 15*R* SiC can be explained by the potential energy of attraction between ionized N donors, and conduction electrons appeared at the high-impurity concentration [38].

Using the deduced above ε_3 value, we can estimate the density of states at the Fermi level $N(E_F)$ as [24]

$$\varepsilon_3 \approx \frac{1}{N(E_F)a_B^3 4\pi/3}, \tag{3}$$

where a_B is the Bohr radius.

The modified Bohr radius value for N donors in 15*R* SiC is 13.9–10.5 Å [45]; therefore, using Eq. (2), the $N(E_F)$ value can be estimated to be in the range from 5.9×10^{22} to 1.4×10^{23} eV$^{-1}\cdot$cm^{-3}.

Considering the high N donor concentration in the studied samples, we suppose the appearance of a VRH process at very low temperatures when the activation energy decreases, and the hopping length rises with the temperature decrease. In this case, a sufficiently high density of localized states close to the Fermi level is expected [39].

B. EPR measurements

At $T > 160$ K, no EPR signals were detected in the samples under study. We have found that the EPR spectrum at $T < 160$ K is dominated by a single line (designated as *S* line) with $S = 1/2$, showing an axial symmetry (C_{3V}) with $g_\perp = 2.0026(2)$ and $g_\parallel = 2.0043(2)$. Figure 3 demonstrates the EPR spectra recorded at $\nu_0 = 328.84$ GHz at $T = 8$ K in 15*R* SiC monocrystals with $(N_D–N_A) \sim 5\times10^{18}$ cm^{-3}. The simulation of EPR spectra allowed us to resolve the *S* line and low-intensity triplets ($S = 1/2$) from N donors residing in $k1$, $k2$, and $k3$ nonequivalent positions ($N_{k1,k2,k3}$) caused by the hyperfine coupling with ^{14}N nuclei ($I = 1$, 99.6%).

As was mentioned above in SiC having $(N_D–N_A) \geqslant 5\times10^{18}$ cm^{-3}, the disappearance of N donors residing in "*h*" positions having more shallow levels in the band gap is expected [46–50] along with the appearance of the single line caused by the exchange interaction between N donors. Therefore, no EPR lines from $N_{h1,h2}$ are observed in our 15*R* SiC monocrystals. It should be noted that in 6H SiC, three types of the exchange *S*1, *S*2, and *S*3 lines were observed in high-frequency EPR spectra ($\nu_0 = 140$ GHz) with corresponding *g*-factor values [49]: $g_\perp = 2.0031(2)$, $g_\parallel = 2.0045(2)$ (*S*1 line); $g_\perp = 2.0031(2)$, $g_\parallel = 2.0042(2)$ (*S*2 line); $g_\perp = 2.0031(2)$, $g_\parallel = 2.0039(2)$ (*S*3 line). The $g_\parallel$ value of *S*1 and *S*2 lines, which were observed in the sample with $(N_D–N_A) \sim 3\times10^{18}$ cm^{-3}, corresponding to the average value of that of N substituting *h* and $k1$ and *h* and $k2$ positions, respectively, while the $g_\parallel$ value for *S*3 line, which was observed in the 6H SiC crystal with $(N_D–N_A) \sim 7\times10^{18}$ cm^{-3}, corresponds to the average value of that of N substituting $k1$ and $k2$ positions. The reason for the differences in the position of the *S* line in 6H SiC and 15*R* SiC can be explained by the higher N concentration in 15*R* SiC and the Fermi-level position at N_{k1} energy level and, as a result, the absence of EPR lines caused by the N substituting *h* positions in EPR spectra of 15*R* SiC.

The single *S* line was recently reported in high-frequency EPR spectra of 15*R* SiC monocrystals having $(N_D–N_A) \sim 5\times10^{18}$ cm^{-3} [25] and was supposed to be due to the exchange interaction of N donors. The EPR spectra of low intensity from N donors residing in cubic positions $k1$, $k2$, and $k3$ ($N_{k1,k2,k3}$) at $T < 80$ K were observed as well. The EPR parameters of paramagnetic centers observed in 15*R* SiC monocrystals with different N donor concentrations are represented in Table I.

Figure 4 shows the temperature dependence of *X*-band EPR spectra in the investigated crystals from 295 to 5 K. No EPR

TABLE I. EPR parameters of paramagnetic centers observed in 15*R* SiC monocrystals with different N donor concentrations.

Center	N_{k1}	N_{k2}	N_{k3}	N_{h1}	N_{h2}	*S* line
$g_\perp$	2.0026(2)	2.0030(2)	2.0030(2)	2.0028(2)	2.0023(2)	2.0026(2)
$g_\parallel$	2.0040(2)	2.0037(2)	2.0038(2)	2.0035(2)	2.0031(2)	2.0043(2)
$A_\perp$ (MHz)	33.6	33.32	30.36	1.1	1.4	
$A_\parallel$ (MHz)	33.6	33.32	30.36	2.1	2.2	
Temperature range	$T < 80$ K	$T < 80$ K	$T < 80$ K	$T < 20$ K	$T < 20$ K	$T < 160$ K
$(N_D–N_A)$ (cm^{-3})	10^{17}–5×10^{18}	10^{17}–5×10^{18}	10^{17}–5×10^{18}	$<10^{18}$	$<10^{18}$	5×10^{18}
Reference	[7, 8, this work]	[7, 8, this work]	[7, 8, this work]	[7]	[7]	[25, this work]

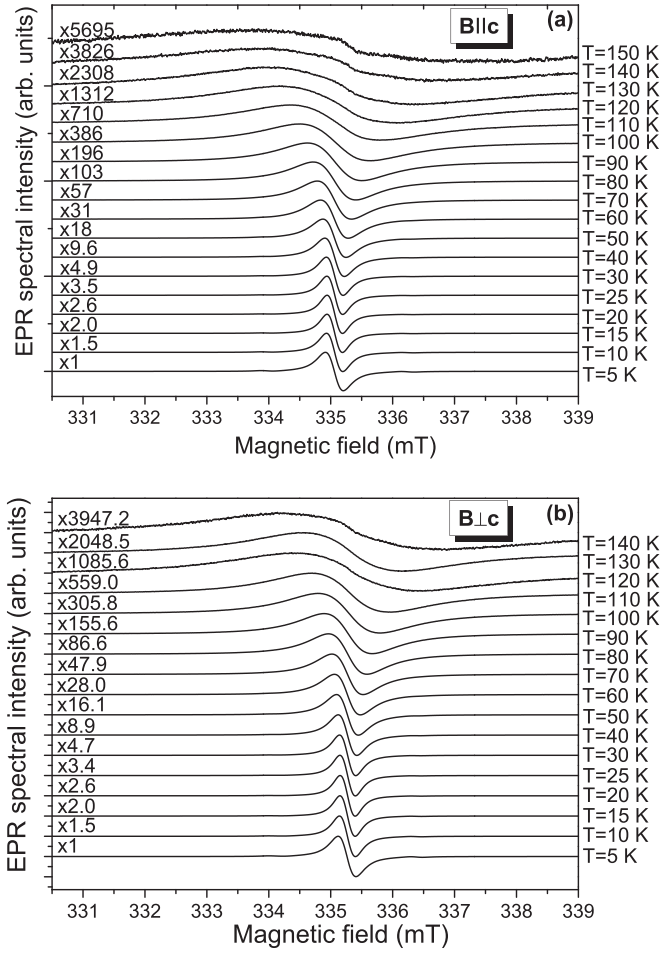

FIG. 4. Temperature dependence of *X*-band EPR spectra measured in 15*R* SiC monocrystals with $(N_D–N_A) \sim 5\times10^{18}$ cm^{-3} at $\mathbf{B}\|\mathbf{c}$ (a) and $\mathbf{B}\perp\mathbf{c}$ (b), $\nu_0 = 9.398$ GHz.

spectra were observed at $T > 170$ K in 15*R* SiC monocrystals with $(N_D–N_A) \sim 5\times10^{18}$ cm^{-3}. The EPR spectrum of the *S* line is observed at $T < 160$ K and has temperature-dependent resonance magnetic field position, line asymmetry, intensity, and linewidth. The EPR spectra of low intensity from $N_{k1,\,k2,\,k3}$ are also observed at $T < 80$ K.

The temperature dependence of the double-integral intensity of *S* line being proportional to the spin susceptibility (χ_{EPR}) was analyzed in the temperature interval from 5 to 160 K. Figure 5 demonstrates the temperature dependence of χ_{EPR} value normalized on its minimum value at 160 K, $\chi_{EPR}(T = 160\,\mathrm{K})$, along with the reciprocal spin susceptibility, $1/\chi_{EPR}$. One can see that the temperature dependence of $1/\chi_{EPR}$ shows a linear trend at low temperatures, whereas, at $T > 90$ K, there is significant curvature due to temperature-independent contribution to the spin susceptibility (χ_0). In this case, for the fitting of the experimental data, the modified form of Curie-Weiss law should be used [51]:

$$\chi_{EPR}(T) = \frac{C}{T-\theta} + \chi_0, \tag{4}$$

$$\chi_{EPR}^{-1}(T) = \frac{T-\theta}{\chi_0(T-\theta)+C}, \tag{5}$$

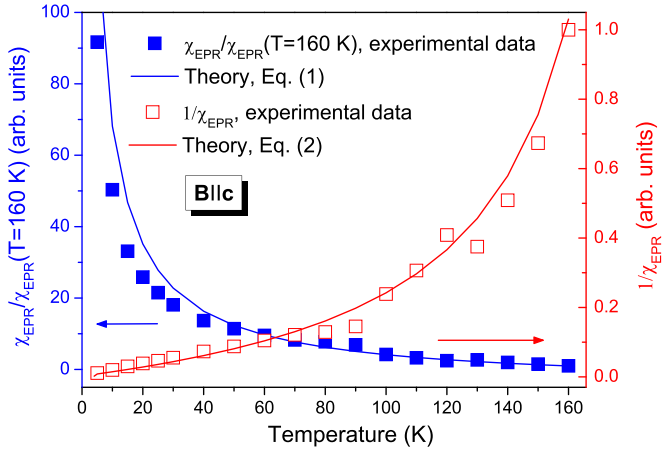

FIG. 5. Temperature variation of spin susceptibility obtained from the analysis of *X*-band EPR *S* line obtained for 15*R* SiC monocrystals with $(N_D–N_A) \sim 5\times10^{18}$ cm^{-3}, $\mathbf{B}\|\mathbf{c}$. Dots are experimental data; solid blue and red lines correspond to the result of fitting with Eqs. (4) and (5).

where C is the Curie constant and θ is the Curie-Weiss temperature in K.

We suppose that the origin of the temperature-independent contribution to the spin susceptibility χ_0 is related to the Pauli paramagnetism that occurs at higher temperatures due to nonlocalized conduction electrons and depends on the density of states at the Fermi energy. At the same time, the Curie-Weiss paramagnetism observed at low temperatures is associated with localized electrons. Fitting of Eqs. (4) and (5) with experimental data from Fig. 5 allowed us to obtain $\theta = -2$ K, which hints at the weak antiferromagnetic coupling in the spin system.

The EPR line shape of the *S* line turned out to be purely symmetric Lorentzian at $T < 90$ K, while at $T > 90$ K it starts to be asymmetric. Such an asymmetry in the line shape takes place when the skin-layer thickness is equal or even thinner concerning the typical size of the investigated crystal caused by the conductivity increase. As a result, the diffusion time of the charge carrier through the skin layer is much shorter than the spin-relaxation time. In this case, the Dysonian line shape with the typical *A*/*B* asymmetry ratio appears in the EPR spectrum [52,53]. The Dysonian line shape is characterized by the dispersion and absorption components, and its first derivative can be written in the general case as [54]

$$\frac{dI}{dB} = A\frac{2x}{(1+x^2)^2} + D\frac{1-x^2}{(1+x^2)^2}, \tag{6}$$

where $x = 2(B-B_0)/\sqrt{3}\Delta B^L_{pp}$, ΔB^L_{pp} is the peak-peak width of the Lorentzian line, and B_0 is the resonance magnetic field position.

From Refs. [55,56], it is known that when the skin layer forms on the flat plate having thickness $2d$, the A and D coefficients in Eq. (6) can be expressed as

$$A = \frac{\sinh p + \sin p}{2p(\cosh p + \cos p)} + \frac{1+\cosh\cos p}{(\cosh p + \cos p)^2},$$

$$D = \frac{\sinh p - \sin p}{2p(\cosh p + \cos p)} + \frac{\sinh p \sin p}{(\cosh p + \cos p)^2}, \tag{7}$$

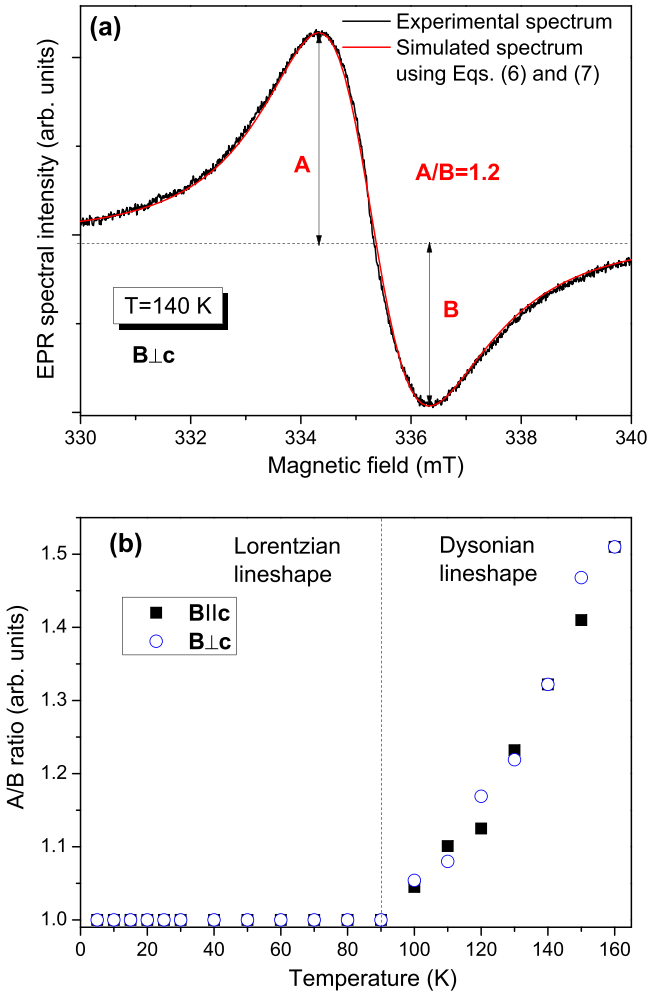

FIG. 6. (a) Result of the fitting of experimental X-band EPR spectrum from S line in 15R SiC monocrystals having $(N_D–N_A) \sim 5\times10^{18}\,\mathrm{cm}^{-3}$ using Dysonian line shape by Eq. (6) and Eq. (7). $T = 140$ K, $\mathbf{B}\perp\mathbf{c}$. (b) Temperature variation of the A/B ratio of the S line obtained from the fitting of X-band EPR spectra in 15R SiC monocrystals having $(N_D–N_A) \sim 5\times10^{18}\,\mathrm{cm}^{-3}$ using Eqs. (6) and (7) at $\mathbf{B}\|\mathbf{c}$ (solid squares) and $\mathbf{B}\perp\mathbf{c}$ (open circles).

where $p = 2d/\delta$, $\delta = \sqrt{2/\mu_0\nu\sigma_{ac}}$ is the thickness of the skin layer, μ_0 is the vacuum×magnetic permeability, σ_{ac} is the intrinsic conductivity. The A/B ratio is related to A and D coefficients: $A/B = 1 + 1.5 \cdot D/A$. The Lorentzian line shape corresponds to the case when $A/B = 1$ and $D/A = 0$.

The fitting of the experimental EPR spectrum from S line in 15R SiC monocrystals having $(N_D–N_A) \sim 5\times10^{18}\,\mathrm{cm}^{-3}$ measured at $T = 140$ K and $\mathbf{B}\perp\mathbf{c}$ described by Dysonian line shape utilizing Eqs. (6) and (7) are shown in Fig. 6(a). Using the same approach, we have fitted the EPR spectra of the S line in the wide temperature interval from 5 to 160 K and obtained the temperature variation of the A/B ratio [see Fig. 6(b)]. The observed increase in the A/B ratio (proportional to ac conductivity [57]) agrees with the increase of the MW conductivity (see Fig. 2) at $T = 100$–200 K due to transitions of electrons from N donor energy levels to the conduction band.

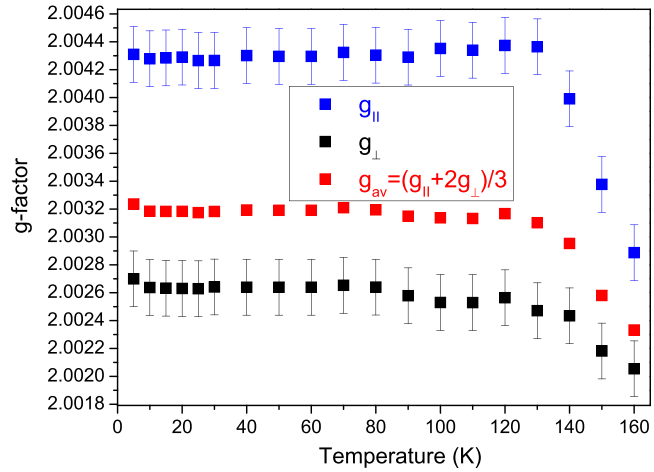

FIG. 7. Temperature dependence of $g_\|$, $g_\perp$, and averaged g values (g_{av}) for S line obtained in 15R SiC monocrystals with $(N_D–N_A) \sim 510^{18}\,\mathrm{cm}^{-3}$ from the fitting of X-band EPR spectra using Eqs. (6) and (7).

Figure 7 represents the temperature dependence of $g_\|$, $g_\perp$, and average g-factor ($g_{av} = 2g_\perp + g_\|)/3$) values obtained from the fitting of EPR spectra in 15R SiC monocrystals having $(N_D–N_A) \sim 5\times10^{18}\,\mathrm{cm}^{-3}$ with Eqs. (6) and (7). One can see from Fig. 7 that at $T > 120$ K, the g-factor values decrease, and the g_{av} value reaches the free-electron value of 2.0023 at $T = 160$ K. Thus, we may assume that at $T > 120$ K, the interaction between exchange-coupled N donors and conduction electrons takes place.

The temperature dependence of the S-line EPR width was obtained from the fitting of Eqs. (6) and (7) with the experimental spectra, when the magnetic field was oriented perpendicular and parallel with respect to the **c** axis, is shown in Fig. 8. From the inset in Fig. 8(a), it is seen that starting from 5 K, the S line narrows with increasing temperature and reaches its minimum value at 20 K, and broadens at $T > 20$ K. The S-line EPR broadening can be related to the appearance of the VRH process in the sample and can be described by the following expression:

$$\Delta B_{pp}(T) = \Delta B_\infty \exp((T_0/T)^{1/4}), \tag{8}$$

where ΔB_∞ is the EPR linewidth at $T \to \infty$, and T_0 is the average height of the barrier for the hopping process [58]. Fitting the experimental data in Fig. 8(b) with Eq. (8) gives us $T_0 = 0.35$ meV.

In the temperature interval from 20 to 160 K, the Orbach relaxation mechanism was used to describe the experimental data from Fig. 8(a):

$$\Delta B_{pp} = A_0 + AT^3 + BT^5 + D\exp(-\Delta_l/k_BT), \tag{9}$$

where A_0 is the residual linewidth (at $T = 20$ K), A and B are related to two-phonon nonresonant relaxation processes, and D is due to resonant two-phonon exchange process, separated from an excited vibronic level Δ_l, e.g., Δ_l is the splitting between the ground state and an excited vibronic level.

Fitting of Eq. (9) with experimental data represented in Fig. 8(a) gave us the Δ_l values as 6.5 meV ($\mathbf{B}\perp\mathbf{c}$) and 4.8 meV ($\mathbf{B}\|\mathbf{c}$) that agree well with the valley-orbit

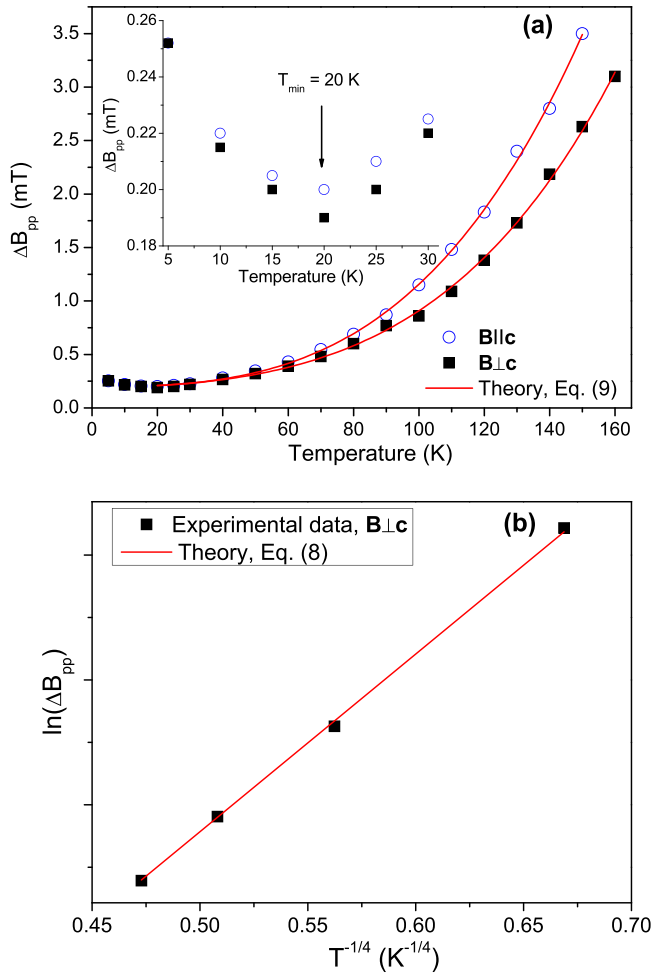

FIG. 8. (a) Temperature variation of the S-line width obtained from the fitting of X-band EPR spectra in 15R SiC monocrystals having $(N_D–N_A) \sim 5\times10^{18}\,\mathrm{cm}^{-3}$ using Eqs. (6) and (7). Open blue circles are experimental data at $\mathbf{B}\|\mathbf{c}$, solid black squares are experimental data at $\mathbf{B}\perp\mathbf{c}$, and solid red lines are fitting with Eq. (9). Inset shows the temperature range of the EPR linewidth minimum at 20 K for both principal magnetic field orientations. (b) Natural logarithm of ΔB_{pp} vs $T^{-1/4}$ in the temperature interval from 5 to 20 K. Solid black squares are experimental data at $\mathbf{B}\perp\mathbf{c}$; solid red line is fitting with Eq. (8).

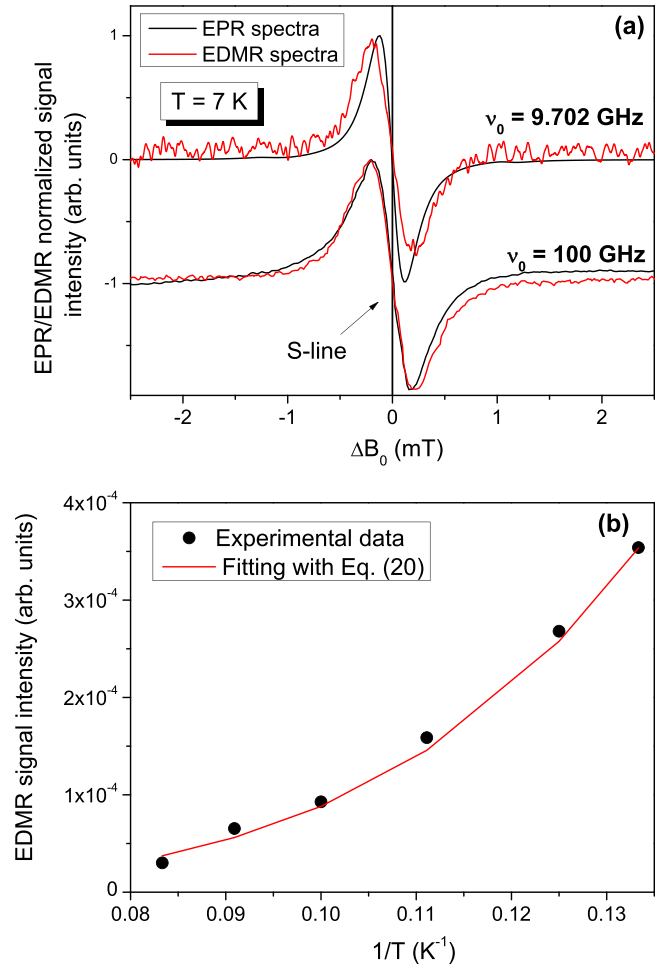

FIG. 9. (a) Comparison of EPR and EDMR spectra of S line measured in 15R SiC monocrystals having $(N_D–N_A) \sim 5\times10^{18}\,\mathrm{cm}^{-3}$ at $\nu_0 = 9.702$ GHz and $\nu_0 = 100$ GHz, $T = 7$ K, $\mathbf{B}\perp\mathbf{c}$. (b) Temperature variation of EDMR spectra intensity of S line measured at $\nu_0 = 100$ GHz, $\mathbf{B}\perp\mathbf{c}$, The solid line results from the fitting with Eq. (20).

splitting values of 1s N donor ground state in 15R SiC with $(N_D–N_A) \sim 2\times10^{18}\,\mathrm{cm}^{-3}$ reported from Raman-scattering measurements (4.7, 7.4, and 12.1 meV) in Ref. [56].

As a result, we can summarize that the S-line EPR signal in 15R SiC monocrystals having $(N_D–N_A) \sim 5\times10^{18}\,\mathrm{cm}^{-3}$ should be related to the exchange interaction of N donors. Previously in highly N-doped 6H and 4H SiC, the exchange line due to the exchange coupling of N donors residing in cubic and hexagonal positions was observed at $T < 20$ K only (the temperature interval for the observation of N_h EPR line in low N-doped samples). In our case, we observe the S line in the EPR spectrum in a wide temperature range. Considering the g-factor values obtained for S line (see Table I), we may suppose that the S line is related to the exchange interaction between identical N_{k1} donors having the deepest energy level and highest N concentration. Nevertheless, in the VRH regime, the interaction between N substituting hexagonal and quasicubic sites could also occur.

C. EDMR measurements

The EDMR measurements were performed in the temperature range from 295 to 4.2 K at $\nu_0 = 9.702$ GHz and $\nu_0 = 100$ GHz. A single EDMR signal was observed in the temperature interval from 20 to 4.2 K [see Fig. 9(a)] with the same g factor as that of the S line observed in the EPR spectrum [$g_\perp = 2.0026(3)$, $g_\| = 2.0043(3)$] and therefore was related to it. A similar single EDMR signal was reported previously in 15R SiC monocrystals having $(N_D–N_A) \sim 5\times10^{18}\,\mathrm{cm}^{-3}$ at $T < 12$ K and $\nu_0 = 100$ GHz and also attributed to the exchange-coupled N donors [24]. The EDMR signal intensity of the S line decreases with the temperature; its dependence is shown in Fig. 9(b).

Let us consider the models which can be responsible for the appearance of the EDMR signal from the S line at $T < 20$ K in the VRH regime in 15R SiC. It is well known that all acceptors

are negatively charged at low temperatures in compensated semiconductors of n type, while some donors are neutral and contain electrons, and others are positively charged (empty). The conductivity occurs because there is an empty state above the Fermi level, allowing electrons from nearby occupied states (below the Fermi level) to get energy from the phonon and move. This effect is related to a hopping process leading to net electrical conductivity when we apply the electric field. The hopping probability of an electron jumping from a position "i" to a nearby position "j" can be expressed as a function of the distance between these positions (R_{ij}) and their potential energy difference ε_{ij} [24,42]:

$$W_{ij}(R_{ij}) = \nu_{ph} \exp[-2\alpha R_{ij} - \varepsilon_{ij}/k_B T], \qquad (10)$$

where $\nu_{\rm ph}$ is the phonon distribution and $\alpha = 1/a_{\rm B}$ is the radius of the wave function of localization states. The case when $\varepsilon_{ij}/k_B T << 2\alpha R_{ij}$ corresponds to nearest-neighbor hopping (a carrier hops from one site to the next-nearest site obtaining the needed energy from a phonon), while the case of $\varepsilon_{ij}/k_B T > 2\alpha R_{ij}$ corresponds to the VRH process occurring at low temperatures.

According to Ref. [24], the primary mechanism causing the EDMR signal in highly doped semiconductors with donor concentration close to but lower than the critical one ($N_{\rm crit}$) for semiconductor-to-metal transition (for 15R SiC $N_{\rm crit} \sim (0.24/a_B)^3 = 1.2\times10^{19}$ cm^{-3}, $a_{\rm B} = 10.5$ Å) is EPR-induced hopping, including EPR-energy transfer and spin-flip hops processes.

The EPR-energy transfer model [59] corresponds to the situation when the localized electron at the site i is excited to the upper Zeeman level by adsorption of MW energy. Afterward, the localized electron at the Fermi level moves from site j to site k (located above the Fermi level) by exchange interaction with the electron at position i. EPR-energy transfer process occurs when singly and doubly occupied states are present. Furthermore, a hop to an occupied state is only possible if the electron spins are antiparallel. In our samples, the hopping process occurs between N states, which can be either unoccupied or singly occupied. Therefore, the EPR-energy transfer model can not be responsible for the low-temperature EDMR signal detected in 15R SiC crystals.

The spin-flip hops model [60] is described by the hopping process occurring between occupied states and thus is spin dependent: an electron can only hop to sites occupied by an electron with antiparallel spin orientation. First, the electron at the site i is excited to the upper Zeeman level by absorbing a MW photon. Then there are two processes contributing to spin relaxation. The first process corresponds to typical spin-lattice relaxation: the electron returns to the lower Zeeman level emitting a phonon of energy $h\nu_{\rm phonon}$ equal to $h\nu_{\rm MW}$. The second process occurs when an electron hops to a neighboring ionized donor j reversing its spin and emitting a phonon of energy equal to ($h\nu_{\rm MW}$–$\Delta\varepsilon$), where $\Delta\varepsilon$ is the potential energy difference of i and j donors.

Another mechanism can also contribute to conductivity: the electron at the site i is excited to the upper Zeeman level, and then the hop to site $j*$ is accompanied by a spin flip since the required energy was reduced. This process occurs when the potential-energy difference of i and $j*$ is comparable to EPR energy $h\nu_{\rm MW}$. The probability of finding sites with antiparallel spin orientations is increased by spin flips enhancing the hopping process. In this case, the hopping time should be much shorter than the spin-lattice relaxation time.

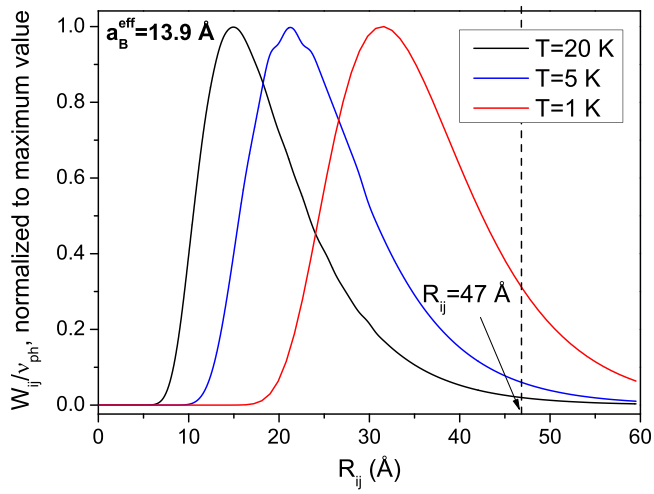

FIG. 10. Theoretical estimation of hopping probability (W_{ij}) vs distance between donors R_{ij} at different temperatures (T = 20, 5, and 1 K) using Eq. (10) for 15R SiC monocrystals having ($N_{\rm D}$–$N_{\rm A}$) $\sim 5\times10^{18}$ cm^{-3}. Curves were normalized to their maximum value.

On the other hand, according to Refs. [59,60], the relative resistivity decrease for the spin-flip hopping mechanism is expected to be $|\Delta\rho_{\rm EPR}/\rho| \leqslant 10^{-2}$ ($\Delta\rho_{\rm EPR}$ is absolute resonant resistivity change at resonance conditions, i.e., EDMR signal amplitude), while for the EPR energy transfer mechanism, it should be $|\Delta\rho_{\rm EPR}|/\rho \leqslant -10^{-4}$. At the same time, it was reported in Ref. [61] for EDMR signal originated from the spin-dependent recombination in Si that the resistivity enhancement is $\Delta\rho_{\rm EPR}/\rho = +10^{-4}$. Our data measured at $\nu_0 = 9.7$ GHz, $T = 7$ K, and $U = 3$ V give $\Delta\rho_{\rm EPR}/\rho = -4.1\times10^{-3}$, which is close to the value obtained for the 6H SiC crystals in Ref. [24] ($\Delta\rho_{\rm EPR}/\rho \sim -10^{-3}$). Thus, we can conclude that the EPR energy transfer and spin-dependent recombination mechanisms are not responsible for low-temperature EDMR signal in 15R SiC monocrystals.

Another mechanism leading to the additional hopping has been discussed for 6H SiC [24]: resonant MW absorption that can occur at very low temperatures in the VRH mode. According to this model, an electron at the site i can jump to the unoccupied site j by absorbing a MW photon, resulting in an energy separation between both sites equal to the photon energy: $\varepsilon_{ij} = h\nu_0 (\varepsilon_{ij} \approx 3.89\times10^{-5}$ eV for $\nu_0 = 9.4$ GHz). For this ε_{ij} value, there is a definite number of N donor pairs composed of one ionized donor j and one neutral i donor with an energy difference approximately equal to MW energy.

It is known that the average energy distance ε_{ij} in the VRH regime can be expressed as [58] $\varepsilon_{ij} \approx (N(E_F)R_{ij}^3 4\pi/3)^{-1}$; therefore, using estimated above $N(E_{\rm F})$ values as 5.9×10^{22} eV^{-1} cm^{-3} (for $a_{\rm B} = 13.9$ Å), one can obtain the corresponding hopping distance: $R_{ij} \approx 47$ Å $\sim 3 \cdot a_{\rm B}$. The fact that R_{ij} is larger than the average distance between N donors can be explained by the fact that $\varepsilon_{ij} \ll \varepsilon_3$.

Figure 10 demonstrates the theoretical variation of hopping probability W_{ij} versus $R_{\rm ij}$ using Eq. (10) and

$\varepsilon_{ij} \approx (N(E_F)R_{ij}^3 4\pi/3)^{-1}$ at $T = 20$, 5, and 1 K. It can be observed that the curve at $T = 1$ K corresponds to the maximum W_{ij} value at hopping distance ~30 Å. Therefore we can conclude that the photon-induced hopping contributes to EDMR signal in our samples only at $T < 1$ K.

According to Ref. [24], the explanation for the occurrence of EDMR spectra in the hopping regime could be the heating of the N donor electrons under EPR resonance conditions: the spin system adsorbs MW energy, which is then transferred to the surroundings through the spin-lattice relaxation process and the temperature of the crystal rises. So, if the MW energy is absorbed in the crystalline sample, it is converted into heat, increasing the sample temperature. Therefore, the specific heat must also be considered in addition to the adsorbed MW power. The temperature rise (ΔT) caused by the MW power absorption during a time (t) is given by [24]

$$\Delta T = \frac{\int_0^t P_{\mathrm{MW}} dt}{m c_V}, \tag{11}$$

where P_{MW} is the MW power, c_{V} is the specific-heat capacity, and m is the sample mass.

At resonance conditions, the spin system will adsorb the MW energy P_{EPR} that is afterward transferred to the lattice surroundings via the spin-lattice relaxation process. Therefore, the crystal temperature increases at resonance, and it can cause the observed decrease of EPR-induced resistivity ρ_{EPR}.

In order to estimate the magnitude of the temperature variation induced by the absorption of MW at magnetic resonance conditions, the MW absorbed by resonance at the temperature and MW attenuation conditions should be calculated. For a system with $S = 1/2$, the MW power absorbed by the spins at resonance is expressed as [62]

$$P_{\mathrm{EPR}} = \frac{1}{4}\gamma^2 B_1^2 h\nu_0 n_0 f(\nu_0) \times \frac{1}{1 + \frac{1}{4}\gamma^2 B_1^2 f(\nu_0)/\left\{\frac{1}{2}(W_{12} + W_{21})\right\}}, \tag{12}$$

where B_1 is the MW magnetic field, γ is the gyromagnetic ratio of the paramagnetic defect, n_0 is the thermal equilibrium value of population difference, $f(\nu_0)$ is the line-shape function, W_{12} and W_{21} are the transition rates from the lower Zeeman level to the upper one, and vice versa.

The Lorentzian line-shape function can be expressed as [62]

$$f(\nu) = \frac{2T_2}{1 + (\gamma B_0 - 2\pi\nu_0)^2 T_2^2}, \tag{13}$$

where T_2 is transverse relaxation time describing the spin-spin relaxation.

Using the relationship $W_{12} + W_{21} = 1/T_1$, where T_1 is the longitudinal relaxation time describing the spin-lattice relaxation, we can assume that

$$P_{\mathrm{EPR}} = \frac{1}{4}\gamma^2 B_1^2 h\nu_0 n_0 f(\nu) \cdot \frac{1}{1 + \frac{1}{2}\gamma^2 B_1^2 T_1 f(\nu_0)}. \tag{14}$$

In the nonsaturation case, the second factor can be neglected, and Eq. (14) can be rewritten as

$$P_{\mathrm{EPR}} \approx \tfrac{1}{4}\gamma^2 B_1^2 h\nu_0 n_0 f(\nu_0). \tag{15}$$

In our experiment, we have estimated the average B_1 value, which comes from smooth-wall waveguide MW aperture, as 7.299×10^{-6} T at a MW power level of 125 mW. Applying Bloch equations, the T_2 time from the EPR peak-to-peak linewidth recorded by CW EPR can be expressed as [63] $T_2 = \frac{2}{\sqrt{3}\gamma\Delta B_{pp}}$, which allows us to calculate the line-shape function at the absorption maximum at 100 GHz as $f(\nu_0) = 1.6\times10^{-16}$. As a result, Eq. (15) gives us the value for the maximum absorbed power: $P_{\mathrm{EPR}} = 1.696\times10^{-8}\,\mathrm{J\,s^{-1}}$. Thus, using Eq. (11) for an integration time of 1 s, we can estimate the EPR-induced temperature increase at $T = 7$ K, $P_{\mathrm{MW}} = 125$ mW: $\Delta T_{\mathrm{EPR}} = 5.9\times10^{-3}$ K, giving us the value of maximum temperature variation that can be induced at resonance conditions during a time of 1 s. The obtained value of ΔT_{EPR} is comparable to that obtained in Ref. [24] for 6H SiC crystals: $\Delta T_{\mathrm{EPR}} = 2.3\times10^{-3}$ K.

As it follows from Eq. (11), the specific heat should be considered besides the absorbed MW power. It is well known that the specific heat is temperature dependent and changes with SiC polytype and doping level [64–66], and the temperature variation of the specific-heat capacity for 15*R* SiC at low temperatures reveals the T^3 behavior [64]. The MW power absorbed by the sample at resonance condition varies with the temperature via the spin-lattice relaxation time [24]: $T_1 \propto T^3$, where $m = -1$ for the direct relaxation process and $m = -5$, -7, and -9 for the indirect one. The temperature variation of P_{EPR} is much weaker than that of the specific heat. Thus, the temperature variation of the EPR-induced temperature increase should be governed by the specific-heat temperature dependence $c_{\mathrm{V}} \propto T^3$ [24]:

$$\Delta T(T) = \frac{\int_0^t P_{\mathrm{EPR}} dt}{m c_V(T)} \propto \frac{\int_0^t P_{\mathrm{EPR}} dt}{T^3}. \tag{16}$$

The corresponding resistivity decrease will depend on the dominant charge process at the respective temperature. For the VRH regime, the temperature variation of the resistivity is described as $\rho(T) = \rho_0 \exp[(T_0/T)^{1/4}]$; therefore, the resistivity decrease caused by MW absorption at resonance conditions can be written for a small temperature change ΔT as [24]

$$\Delta\rho(T) = \frac{\delta\rho}{\delta T}\Delta T = -\frac{\rho_0 T_0^{1/4}}{4}\frac{1}{T^{5/4}}\exp((T_0/T)^{1/4})\Delta T. \tag{17}$$

Using Eq. (11) one can obtain the expression for the resistivity decrease per integration time Δt for the VRH regime [24]:

$$\frac{\Delta\rho}{\Delta t} = -\frac{\rho_0 T_0^{1/4}}{4}\frac{P_{\mathrm{EPR}}}{m c_V}\frac{1}{T^{5/4}}\exp((T_0/T)^{1/4}). \tag{18}$$

Assuming that $c_{\mathrm{V}} \propto T^3$ and neglecting the temperature dependence of MW power absorbed at resonance P_{EPR}, we can obtain from Eq. (18) that [24]

$$\frac{\Delta\rho}{\Delta t} = -c_0 T^{-17/4}\exp((T_0/T)^{1/4}), \tag{19}$$

where c_0 contains temperature-independent terms.

Thus, using the same approach as in Ref. [24] for 6H SiC and considering that the temperature variation of the

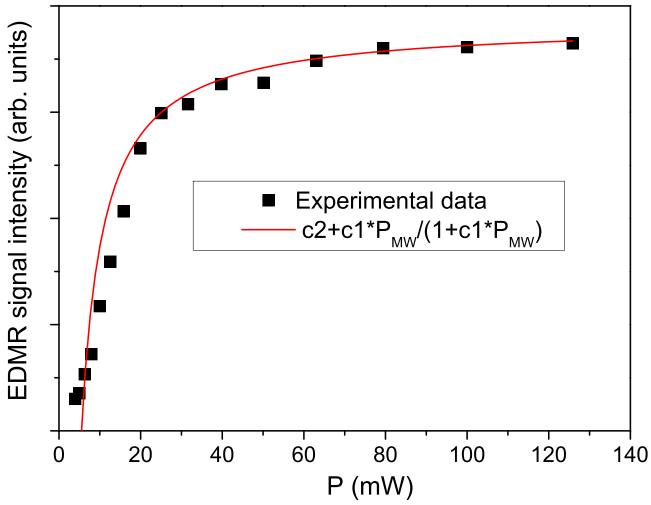

FIG. 11. Power dependence of the S-line EDMR signal amplitude measured in 15R SiC monocrystals having $(N_D–N_A) \sim 5\times10^{18}$ cm^{-3} at $\nu_0 = 100$ GHz and $T = 7$ K. Dots are experimental data; the solid line is the result of fitting with Eq. (21).

specific-heat capacity for 15R SiC at low temperatures reveals the T^3 behavior [64], we can express the observed temperature variation of the EDMR signal intensity in the VRH mode as

$$I_{\mathrm{EDMR}}(T) \propto T^{-17/4} \exp((T_0/T)^{1/4}). \tag{20}$$

We have obtained a good agreement of the experimental data represented in Fig. 9(b) using Eq. (20) with the T_0 value of 1.7 meV, which is close to the value obtained above from the analysis of the temperature variation of the S-line EPR width (0.35 meV). Thus, we can conclude that the experimentally obtained temperature dependence of the S-line EDMR signal is related to the EPR-induced heating effect.

As shown in Fig. 11, the S-line EDMR signal amplitude increases linearly to 25 mW and remains constant for higher MW power levels. This process can be expressed theoretically by the following law [67]:

$$I_{\mathrm{EDMR}} = c_2 + c1P_{\mathrm{MW}}/(1 + c1P_{\mathrm{MW}}), \tag{21}$$

where P_{MW} is the MW power level, and $c1$ and $c2$ are the fitting parameters.

The observed temperature behavior of the S-line EDMR signal amplitude is consistent with the heating effect and energy-transfer mechanism.

Thus, we can conclude that analogous to 6H SiC [24], the EPR-induced temperature-increase mechanism and spin-flip hops process are responsible for the appearance of the S-line EDMR signal in the VRH regime in 15R SiC monocrystals having $(N_D–N_A) \sim 5\times10^{18}$ cm^{-3}. Figure 12 shows the corresponding model for this process. First, the spin system absorbs the photon energy and afterward loses it due to diffusion to the lattice. The energy is transferred from the MW source to the investigated crystal and then transferred to the environment. When no heat-removal mechanisms are present, conductivity grows with the sample temperature. Also, the spins can lose the MW energy directly at the Fermi level (hopping), leading to the rise of conductivity.

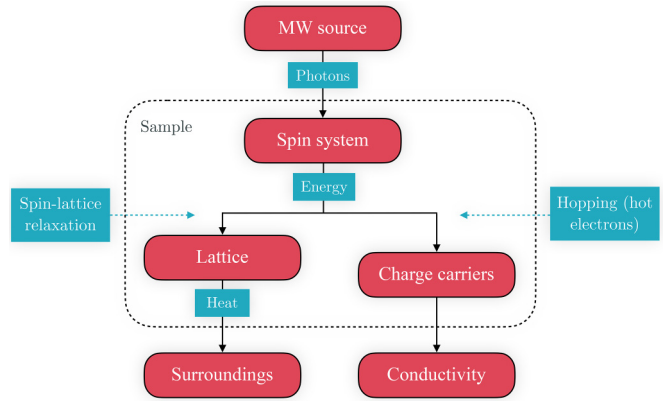

FIG. 12. (Adapted from Ref. [24]) Mechanism responsible for the appearance of S-line EDMR signal in the VRH regime in 15R SiC having $(N_D–N_A) \sim 5\times10^{18}$ cm^{-3}.

IV. CONCLUSIONS

The electronic and magnetic properties of 15R SiC monocrystals with a nitrogen donor concentration $(N_D–N_A) \sim 5\times10^{18}$ cm^{-3} grown by the modified Lely method were studied by multifrequency EPR and EDMR methods ($\nu_0 = 9.4$ to 328.84 GHz), along with cavity perturbation technique in a wide temperature interval.

The temperature variation of the MW conductivity revealed different processes in highly nitrogen-doped 15R SiC monocrystals: scattering of conduction electrons by ionized donor impurities ($T = 295$–200 K), transitions of electrons from donor energy levels to the conduction band with activation energy $\varepsilon_1 = 30$ meV ($T = 200$–100 K), transition process of electrons between Hubbard bands ($T = 100$–50 K), and electron-hopping process between donor impurity atoms with activation energy $\varepsilon_3 = 1.5$ meV ($T < 50$ K). The density of states at the Fermi level was estimated in the range from 5.9×10^{22} to 1.4×10^{23} eV^{-1} cm^{-3}.

At $T < 160$ K, the EPR spectra recorded in 15R SiC monocrystals having $(N_D–N_A) \sim 5\times10^{18}$ cm^{-3} showed an intense S line with $g_\perp = 2.0026(2)$ and $g_\parallel = 2.0043(2)$ caused by exchange coupling between identical N donors residing at $k1$ nonequivalent position in 15R SiC lattice and having the deepest energy level and highest N concentration. In addition, at $T < 80$ K, the low-intensity triplets due to N donors residing at $k1$, $k2$, and $k3$ nonequivalent positions were detected in EPR spectra.

It was found that there are two contributions to the temperature variation of the S-line spin susceptibility: Pauli-like (temperature independent) and Curie-Weiss (temperature dependent) with $\theta = –2$ K, which hints at the weak antiferromagnetic interaction in the spin system. The EPR line shape of the S line turned out to be purely symmetric Lorentzian at $T < 90$ K, while at $T > 90$ K, it is an asymmetric Dyasonian. The observed increase in the line-asymmetry ratio (proportional to ac conductivity) agrees with the rise of the MW conductivity at $T = 100$–200 K due to transitions of electrons from N donor energy levels to the conduction band.

The analysis of temperature variation of the average g-factor value of the S line allowed us to conclude that the interaction between exchange-coupled N donors and

conduction electrons takes place at $T > 120$ K. The temperature variation of the S-line EPR width at $T \leqslant 20$ K broadens due to the appearance of the VRH process, with the average barrier height for the hopping process of about 0.35 meV. At $T > 20$ K, the Orbach relaxation mechanism takes place with the separation between the ground state and an excited vibronic level of 6.5 meV ($\mathbf{B}\perp\mathbf{c}$) and 4.8 meV ($\mathbf{B}\|\mathbf{c}$) that agrees well with the valley-orbit splitting values of 1s N donor ground state in highly nitrogen-doped 15R SiC.

The EDMR spectra revealed a single S line at $T < 20$ K. We have concluded that the EPR-induced temperature-increase mechanism, along with the spin-flip hops process, are responsible for the appearance of the EDMR signal from the S line in the VRH regime.

ACKNOWLEDGMENTS

A.S. acknowledges the support of the European Research Council (ERC) through the European Union's Horizon 2020 Research and Innovation Program under Grant No. 714850, and by Internal Grant Agency, Grant No. CEITEC VUT-J-19-6070, Czech Republic. O.L. acknowledges the financial support of Grant Agency of the Czech Republic (GAČR) under the Grant No. Standard 23–05578S project. P.N. acknowledges the financial support of Grant Agency of the Czech Republic (GAČR) under Grant No. EXPRO 21–20716X project. D.S. and A.P. are grateful for support from Operational Program Research, Development and Education financed by European Structural and Investment Funds and the Czech Ministry of Education, Youth and Sports (Project No. SOLID21 CZ.02.1.01/0.0/0.0/16 019/0000760). B.N. acknowledges the financial support from the German Science Foundation DFG (Projects No. 410866378 and No. 410866565) and from the German Federal Ministry of Education and Research BMBF (Project DIQTOK, Grant No. 16KISQ034K). The authors also would like to thank Professor Patrick Lenahan (The Pennsylvania State University) for fruitful scientific discussion during manuscript preparation.

[1] R. Schomer, P. Friedrichs, D. Peters, and D. Stephani, Significantly improved performance of MOSFETs on silicon carbide using the 15R-SiC polytype, IEEE Electron Device Lett. **20**, 241 (1999).

[2] S. K. Mourya, A. G. Malik, B. Kumar, and R. Chandra, The role of non-homogeneous barrier on the electrical performance of 15R-SiC Schottky diodes grown by in-situ RF sputtering, Mater. Sci. Semicond. Process. **149**, 106855 (2022).

[3] F. R. Chien, S. R. Nutt, W. S. Yoo, T. Kimoto, and H. Matsunami, Terrace growth and polytype development in epitaxial β-SiC films on α-SiC (6H and 15R) substrates, J. Mater. Res. **9**, 940 (1994).

[4] A. A. Lebedev, P. L. Abramov, E. V. Bogdanova, A. S. Zubrilov, S. P. Lebedev, D. K. Nelson, N. V. Seredova, A. N. Smirnov, and A. S. Tregubova, Study of the 3C-SiC layers grown on the 15R-SiC substrates, Semiconductors **43**, 756 (2009).

[5] Ö. Balcı, M. Buldu, A. U. Ammar, K. Kiraz, M. Somer, and E. Erdem, Defect-induced B_4C electrodes for high energy density supercapacitor devices, Sci. Rep. **11**, 11627 (2021).

[6] E. Erdem, V. Mass, A. Gembus, A. Shulz, V. Liebau-Kunzmann, C. Fasel, R. Riedel, and R. A. Eichel, Defect structure in lithium-doped polymer-derived SiCN ceramics characterized by Raman and electron paramagnetic resonance spectroscopy, Phys. Chem. Chem. Phys. **11**, 5628 (2009).

[7] E. N. Kalabukhova, N. N. Kabdin, S. N. Lukin, E. N. Mokhov, and B. D. Shanina, ESR spectra of nonequivalent nitrogen sites in 15R SiC, Fiz. Tverd Tela **31**, 50 (1989) [Sov. Phys. Solid State **31**, 378 (1989)].

[8] D. Savchenko, E. Kalabukhova, B. Shanina, A. Pöppl, V. Yukhymchuk, J. Lančok, E. Ubyivovk, and E. Mokhov, EPR, ESE, and pulsed ENDOR study of the nitrogen donors in 15R SiC grown under carbon-rich conditions, Phys. Status Solidi B **252**, 566 (2014).

[9] G. Gruber, J. Cottom, R. Meszaros, M. Koch, G. Pobegen, T. Aichinger, D. Peters, and P. Hadley, Electrically detected magnetic resonance of carbon dangling bonds at the Si-Face 4H−SiC/SiO_2 interface, J. Appl. Phys. **123**, 161514 (2018).

[10] T. Umeda, Y. Nakano, E. Higa, T. Okuda, T. Kimoto, T. Hosoi, H. Watanabe, M. Sometani, and S. Harada, Electron-spin-resonance and electrically detected-magnetic-resonance characterization on P_{bC} center in various 4H−SiC(0001)/SiO_2 interfaces, J. Appl. Phys. **127**, 145301 (2020).

[11] C. J. Cochrane, P. M. Lenahan, and A. J. Lelis, An electrically detected magnetic resonance study of performance limiting defects in SiC metal oxide semiconductor field effect transistors, J. Appl. Phys. **109**, 014506 (2011).

[12] J. P. Ashton and P. M. Lenahan, Multiple-photon transitions in electrically detected magnetic resonance measurements of 4H-SiC transistors, Phys. Rev. B **102**, 020101(R) (2020).

[13] T. Umeda, K. Esaki, R. Kosugi, K. Fukuda, T. Ohshima, N. Morishita, and J. Isoya, Behavior of nitrogen atoms in SiC−SiO_2 interfaces studied by electrically detected magnetic resonance, Appl. Phys. Lett. **99**, 142105 (2011).

[14] R. J. Waskiewicz, B. R. Manning, D. J. McCrory, and P. M. Lenahan, Electrically detected electron nuclear double resonance in 4H-SIC bipolar junction transistors, J. Appl. Phys. **126**, 125709 (2019).

[15] E. Higa, M. Sometani, H. Hirai, H. Yano, S. Harada, and T. Umeda, Electrically detected magnetic resonance study on interface defects at nitrided Si-face, a-face, and m-face 4H−SiC/SiO_2 interfaces, Appl. Phys. Lett. **116**, 171602 (2020).

[16] T. Umeda, T. Kobayashi, M. Sometani, H. Yano, Y. Matsushita, and S. Harada, Carbon dangling-bond center (Carbon Pb Center) at 4H−SiC(0001)/SiO_2 interface, Appl. Phys. Lett. **116**, 071604 (2020).

[17] C. J. Cochrane, P. M. Lenahan, and A. J. Lelis, Identification of a silicon vacancy as an important defect in 4H SiC metal oxide semiconducting field effect transistor using spin dependent recombination, Appl. Phys. Lett. **100**, 023509 (2012).

[18] P. M. Lenahan, N. T. Pfeiffenberger, T. G. Pribicko, and A. J. Lelis, Identification of deep level defects in SiC bipolar junction transistors, Mater. Sci. Forum **527–529**, 567 (2006).

[19] Y. Abe, A. Chaen, M. Sometani, S. Harada, Y. Yamazaki, T. Ohshima, and T. Umeda, Electrical detection of TV2a-type silicon vacancy spin defect in 4H-SiC MOSFETs, Appl. Phys. Lett. **120**, 064001 (2022).

[20] J. P. Ashton, B. R. Manning, S. J. Moxim, F. V. Sharov, P. M. Lenahan, and J. T. Ryan, Intermediate spin pair relaxation through modulation of isotropic hyperfine interaction in frequency-swept spin-dependent recombination in 4H-SiC, Appl. Phys. Lett. **120**, 062403 (2022).

[21] N. T. Bagraev, D. S. Gets, E. N. Kalabukhova, L. E. Klyachkin, A. M. Malyarenko, V. A. Mashkov, D. V. Savchenko, and B. D. Shanina, Electrically-detected electron paramagnetic resonance of point centers in 6H-SiC nanostructures, Semiconductors **48**, 1467 (2014).

[22] T. Sato, H. Yokoyama, and H. Ohya, Electrically detected magnetic resonance (EDMR) measurements of bulk silicon carbide (SiC) crystals, Chem. Lett. **35**, 1428 (2006).

[23] J. Cottom, G. Gruber, P. Hadley, M. Koch, G. Pobegen, T. Aichinger, and A. Shluger, Recombination centers in 4H-SiC investigated by electrically detected magnetic resonance and *Ab Initio* modeling, J. Appl. Phys. **119**, 181507 (2016).

[24] M. I. Grasa Molina, EPR-Induced Charge Transport in Highly Doped Crystalline n-Type Silicon Carbide, Ph.D. Dissertation, Paderborn University, Paderborn, Germany (2000).

[25] A. Solodovnyk, D. Savchenko, O. Laguta, and P. Neugebauer, Multifrequency electrically detected magnetic resonance setup based on a sub-THz FraScan spectrometer, IEEE Trans. Instrum. Meas. (to be published).

[26] Y. M. Tairov and V. F. Tsvetkov, Investigation of growth processes of ingots of silicon carbide single crystals, J. Cryst. Growth **43**, 209 (1978).

[27] K. Momma and F. Izumi, VESTA 3 for three-dimensional visualization of crystal, volumetric and morphology data, J. Appl. Crystallogr. **44**, 1272 (2011).

[28] G. L. Harris, *Properties of Silicon Carbide* (IEE, INSPEC, London, 1995).

[29] S. Stoll and A. Schweiger, EasySpin, a comprehensive software package for spectral simulation and analysis in EPR, J. Magn. Reson. **178**, 42 (2006).

[30] H. G. Beljers, Measurements on gyromagnetic resonance of a ferrite using cavity resonators, Physica **14**, 629 (1949).

[31] J. G. Linhart, I. M. Templeton, and R. Dunsmuir, A microwave resonant cavity method for measuring the resistivity of semiconducting materials, Br. J. Appl. Phys. **7**, 36 (1956).

[32] O. Klein, S. Donovan, M. Dressel, and G. Grüner, Microwave cavity perturbation technique: Part I: Principles, Int. J. Infrared Terahertz Millim. Waves **14**, 2423 (1993).

[33] S. Donovan, O. Klein, M. Dressel, K. Holczer, and G. Grüner, Microwave cavity perturbation technique: Part II: Experimental scheme, Int. J. Infrared Terahertz Millim. Waves **14**, 2459 (1993).

[34] M. Godlewski, Microwave conductivity measurements in CdTe, Phys. Status Solidi A **51**, K141 (1979).

[35] W. P. Lee, E. S. Choi, E. B. Park, J. Y. Park, Y. W. Park, C. S. Hwang, and T. W. Kim, Microwave conductivity of alkali-metal doped polyacetylene, Synth. Met. **69**, 75 (1995).

[36] V. R. K. Murthy, in *Microwave Materials* (Springer, Heidelberg, 1994), pp. 100–111.

[37] N. F. Mott and W. D. Twose, The theory of impurity conduction, Adv. Phys. **10**, 107 (1961).

[38] H. Fritzsche, Resistivity and Hall coefficient of antimony-doped germanium at low temperatures, J. Phys. Chem. Solids **6**, 69 (1958).

[39] N. F. Mott, Conduction in glasses containing transition metal ions, J. Non-Cryst. Solids **1**, 1 (1968).

[40] N. A. Poklonskij, *Ionization Equilibrium and Hopping Conductivity in Doped Semiconductors* (Belarus. Gos. Univ., Minsk, 2004) [in Russian].

[41] H. Overhof, Hopping conductivity in disordered solids, Festkörperprobleme **16**, 239 (1976).

[42] A. Miller and E. Abrahams, Impurity conduction at low concentrations, Phys. Rev. **120**, 745 (1960).

[43] A. L. Efros, B. I. Shklovskii, and I. Y. Yanchev, Impurity conductivity in low compensated semiconductors, Phys. Status Solidi B **50**, 45 (1972).

[44] W. C. Mitchel, A. O. Evwaeaye, S. R. Smith, and M. D. Roth, Hopping conduction in heavily doped bulk n-type SiC, J. Electron. Mater. **26**, 113 (1997).

[45] M. Ikeda, H. Matsunami, and T. Tanaka, Site effect on the impurity levels in 4H, 6H, and 15R SiC, Phys. Rev. B **22**, 2842 (1980).

[46] D. V. Savchenko, The electron spin resonance study of heavily nitrogen doped 6H SiC crystals, J. Appl. Phys. **117**, 045708 (2015).

[47] U. Gerstmann, E. Rauls, S. Greulich-Weber, E. N. Kalabukhova, D. V. Savchenko, A. Pöppl, and F. Mauri, Nitrogen donor aggregation in 4H-SiC: G-Tensor calculations, Mater. Sci. Forum **556-557**, 391 (2007).

[48] E. N. Kalabukhova, S. N. Lukin, and O. T. Sergeev, ESR of technological coatings made of silicon carbide, Phys. Solid State **35**, 210 (1993).

[49] E. N. Kalabukhova and S. N. Lukin, EPR spectrum in n-6HSiC at high donor nitrogen concentrations, Low Temp. Phys. **22**, 808 (1996).

[50] E. N. Kalabukhova, S. N. Lukin, and V. S. Kisilev, Hopping conduction effects in the ESR spectra of 6H SiC heavily doped with nitrogen, J. Phys.: Conf. Ser. **142**, 405 (1996).

[51] S. Mugiraneza and A. M. Hallas, Tutorial: A beginner's guide to interpreting magnetic susceptibility data with the Curie-Weiss law, Commun. Phys. **5**, 95 (2022).

[52] G. Feher and A. F. Kip, Electron spin resonance absorption in metals. I. Experimental, Phys. Rev. **98**, 337 (1955).

[53] F. J. Dyson, Electron spin resonance absorption in metals. II. Theory of electron diffusion and the skin effect, Phys. Rev. **98**, 349 (1955).

[54] V. I. Krinichnyi, A. L. Konkin, and A. P. Monkman, Electron paramagnetic resonance study of spin centers related to charge transport in metallic polyaniline, Synth. Met. **162**, 1147 (2012).

[55] A. C. Chapman, P. Rhodes, and E. F. Seymour, The effect of eddy currents on nuclear magnetic resonance in metals, Proc. Phys. Soc. B **70**, 345 (1957).

[56] R. Püsche, M. Hundhausen, L. Ley, K. Semmelroth, G. Pensl, P. Desperrier, P. J. Wellmann, E. E. Haller, J. W. Ager, and U. Starke, Electronic Raman studies of shallow donors in silicon carbide, Mater. Sci. Forum **527-529**, 579 (2006).

[57] Z. Wilamowski, B. Oczkiewicz, P. Kacman, and J. Blinowski, Asymmetry of the EPR absorption line in CdF_2 with Y, Phys. Status Solidi B **134**, 303 (1986).

[58] N. F. Mott, *Conduction in Non-Crystalline Material* (Clarendon Press, Oxford, UK, 1993).

[59] H. Kamimura and N. F. Mott, The variable range hopping induced by electron spin resonance in N-type silicon and germanium, J. Phys. Soc. Jpn. **40**, 1351 (1976).

[60] N. Kishimoto and K. Morigaki, Resistivity decrease due to electron spin resonance in the metallic region of heavily phosphorus-doped silicon, J. Phys. Soc. Jpn **42**, 137 (1977).

[61] B. Stich, S. Greulich-Weber, and J. -M. Spaeth, Electrical detection of electron paramagnetic resonance: New possibilities for the study of point defects, J. Appl. Phys. **77**, 1546 (1995).

[62] G. E. Pake and T. L. Estle, *The Physical Principles of Electron Paramagnetic Resonance*, 2nd ed. (Benjamin, New York, 1973).

[63] C. P. Poole, *Electron Spin Resonance: A Comprehensive Treatise on Experimental Techniques* (Wiley, New York,1983).

[64] W.-W. Xu, F. Xia, L. Chen, M. Wu, T. Gang, and Y. Huang, High-temperature mechanical and thermodynamic properties of silicon carbide polytypes, J. Alloys Compd. **768**, 722 (2018).

[65] D. Morelli, J. Hermans, C. Beetz, W. S. Woo, G. L. Harris, and C. Taylor, Carrier concentration dependence of the thermal conductivity of silicon carbide, J. Phys.: Conf. Ser. **137**, 313 (1993).

[66] I. Parfenova, Y. Tairov, and V. Tsvetkov, Thermal conductivity of silicon carbide in the temperature range 300–3000K, Sov. Phys. Semicond. **24**, 158 (1990).

[67] J.-M. Spaeth, Spin-dependent dynamical processes of excited states in semiconductors, J. Lumin. **66-67**, 462 (1995).